Article:
Mercieca, J., Aram, P., Jones, B.L. et al. (2020) A spatiotemporal estimation framework for real-world LIDAR wind speed measurements. IEEE Transactions on Control Systems Technology, 28 (4). pp. 1595-1602. ISSN: 1063-6536

https://doi.org/10.1109/tcst.2019.2913134

A Spatiotemporal Estimation Framework for Real-World LIDAR Wind Speed Measurements

Julian Mercieca, *Member, IEEE*, Parham Aram, Bryn Ll. Jones, and Visakan Kadirkamanathan, *Member, IEEE*

***Abstract*— Despite significant advances in the remote sensing of fluid flows, light detection and ranging (LIDAR) measurement equipment still presents the problems of having only radial (line-of-sight) wind speed measurements (Cyclops' dilemma). Substantial expanses of unmeasured flow still remain and range weighting errors have a considerable influence on LIDAR measurements. Clearly, more information needs to be extracted from LIDAR data. With this motivation in mind, this brief shows that it is possible to estimate the wind velocity, wind direction, and absolute pressure over the entire spatial region of interest. A key challenge is that most established estimation techniques cater for systems that are finite-dimensional and described by ordinary differential equations (ODEs). By contrast, many fluid flows are governed by the Navier–Stokes equations, which are partial differential-algebraic equations (PDAEs). We show how a basis function decomposition method in conjunction with a pressure Poisson equation (PPE) formulation yields a spatially continuous, strangeness-free, reduced-order dynamic model for which a modified DAE form of the unscented Kalman filter (UKF) algorithm is used to estimate unmeasured velocities and pressure using sparse measurements from wind turbine-mounted LIDAR instruments. The approach is validated for both synthetic data generated from large eddy simulations of the atmospheric boundary layer and real-world LIDAR measurement data. Results show that a reconstruction of the flow field is achievable, thus presenting a validated estimation framework for potential applications including wind gust prediction systems and the preview control of wind turbines.**

***Index Terms*— Differential-algebraic equations, light detection and ranging (LIDAR), Navier–Stokes equations, partial differential equations, unscented Kalman filter (UKF), wind turbines.**

I. Introduction

THE ability to harness fluid flow represents a burgeoning source of renewable energy. However, taking wind as an example, fluid flow is also the main disturbance in the control system of wind turbines. This has sparked recent interest in maximizing energy production and mitigating structural loads using the preview control of wind turbines and forecasting of wind gusts [1]. Although sampling an oncoming wind field has become possible with recent advances in fluid flow measurement, we are still left with the compelling questions of how best to use such limited sparse flow measurements to predict wind gusts and to incorporate such knowledge within a preview control strategy [2]–[4]. Furthermore, these measurements are only line-of-sight velocity measurements and therefore require extra information to resolve wind magnitude and direction (Cyclops' dilemma [5]). Range weighting is another imperfection influencing light detection and ranging (LIDAR) measurements, where a spatial filter is effectively applied along the laser beam, resulting in wind speeds at locations other than the focal distance to affect the measured value [6]. Overcoming such sources of error require further information that may be obtained from a physical model that captures the spatiotemporal dynamics of the wind. This will inevitably rely upon the accuracy of wind models employed and calls for wind velocity estimation tools that predict wind turbine gusts using limited spatiotemporal wind velocity measurements [7], thereby mitigating the possible blade damage due to severe wind gusts if the blade pitch is altered in a timely manner [2], [6]. This would, of course, link measurements to regions of flow which are not directly observed.

Much of the design and control problems treated in the existing wind energy literature take common assumptions that include the steady and uniform flow across the rotor plane [8]. To account for the unsteady nature of fluid flow, the next improvement employs Taylor's frozen turbulence hypothesis [9] that assumes an unchanged spatial structure of wind flow as this advects with a mean velocity [10]. In this brief, we seek to provide a more complete picture of the oncoming wind field by estimating wind velocity and pressure over the horizontal plane spanned by the LIDAR beams, rather than estimating wind flow at only single point locations. This becomes a critical requirement, for instance, in the detection of oncoming flow dynamics having length scales smaller than the wind turbine rotor blade diameter, such as wind gusts. Retaining the full DAE formulation is a very attractive consideration due to the retained pressure field description that is essential for several fluid flow types and situations [11] as well as potential wind flow applications in drag reduction. A pressure difference across a vehicle amounts to pressure drag, which constitutes 80% of ground transportation drag [12].

To conquer the fact that only limited spatial measurements are available, we propose a model-based estimation framework that presents a reasonable approximation where the field is approximated up to a particular bandwidth. We therefore consider models governed by the Navier–Stokes equations, which are known to be a good approximation for many real-world

Manuscript received April 14, 2018; revised January 18, 2019; accepted March 24, 2019. Manuscript received in final form April 20, 2019. The work of J. Mercieca was supported in part by the University of Sheffield Ph.D. Scholarship. The works of P. Aram and V. Kadirkamanathan were supported by the EPSRC Project under Grant EP/K03877X/1. Recommended by Associate Editor Y. Orlov. *(Corresponding author: Julian Mercieca.)*

The authors are with the Department of Automatic Control and Systems Engineering, University of Sheffield, Sheffield, S1 3JD, U.K. (e-mail: julianmercieca@gmail.com; aramparham@gmail.com; b.l.jones@sheffield.ac.uk; visakan@sheffield.ac.uk).

Color versions of one or more of the figures in this paper are available online at http://ieeexplore.ieee.org.

Digital Object Identifier 10.1109/TCST.2019.2913134

fluid flows, including atmospheric boundary layer flow [13], and form the basis of this brief. However, the Navier–Stokes equations are in partial differential-algebraic equation (PDAE) form, which presents difficulties for estimation purposes. In addition to being infinite-dimensional, the DAE formulation (also known as a descriptor or generalized state-space model) means that it is clearly distinguished from constrained ordinary differential equation (ODE) systems. In constrained ODE systems, the evolution of all process states follows differential equations, subject to algebraic constraints that confine state evolution. In DAE systems, however, the evolution of some states is not described by differential equations. Such states are known as algebraic and follow an evolution that is entirely governed by the evolution of differential states, such that all algebraic constraints are satisfied (e.g., pressure in an incompressible flow) [14]. This key difference means that a DAE system cannot be handled and estimated as a constrained ODE system, requiring an alternative estimation scheme [14]. A further important consideration is that DAE systems are generally described by their differentiation index, typically defined as the minimum number of differentiations required in order to obtain an explicit ODE formulation [15]. However, this concept cannot be applied to the Navier–Stokes equations since the pressure is only determined up to an additive constant and the equations are hence of an undetermined nature, which Kunkel and Mehrmann [15] describe in terms of a so-called strangeness index.

The foregoing is particularly challenging since the majority of established estimation techniques are designed for finite-dimensional systems in ODE form. We note that a simplified wind model has been proposed in [16]; however, this is derived as the spatial discretization of the linearized incompressible Navier–Stokes equations. In [5], a simplified deterministic state-space model of atmospheric boundary layer flow was derived based on spatial discretization and excluding pressure. In this brief, we derive a descriptor flow model in nonlinear, spatially continuous form. The key to obtaining a strangeness-free DAE of differentiation index 1 is the reformulation of the Navier–Stokes equations using the pressure Poisson equation (PPE) in conjunction with basis function decomposition. The latter enables the user to represent the flow field by choosing an appropriate number and the placement of basis functions, or states, that are independent of the number and placement of observations, which allows a computationally efficient estimation procedure.

Although estimation for linear descriptor systems has been well developed by several authors, most research efforts in designing observers and filters for the nonlinear case are more recent [17]. The application of Kalman filtering for this class of systems is proposed in [18] for the extended Kalman filter (EKF), while heuristic modifications of the unscented Kalman filter (UKF) [19], [20] are proposed for nonlinear descriptor systems in [21] and [22]. These recent advances in extending Kalman filtering to nonlinear DAE systems assume that the algebraic equations are free of any uncertainty. Although this is generally the case, transforming a nonlinear PDAE to a DAE requires the consideration of model approximation effects. By representing the latter effects stochastically, we compute and exploit the mean and covariance of the algebraic state estimates that are necessary to complete the estimate information obtained and, unlike previous methods, ensure that the mean and covariance of both differential and algebraic states are encoded in the sigma points. We therefore implement a modified DAE form of the discrete-time UKF algorithm, where differential and algebraic state filtering distributions are derived as unscented-transform-based Gaussian approximations. Estimation performance is demonstrated for wind field data generated from large eddy simulations (LESs) of the atmospheric boundary layer, and real-world LIDAR measurement data obtained from a nacelle-mounted LIDAR unit.

In summary, the main contributions of this brief are twofold as follows.

1) The incompressible Navier–Stokes equations are used to model and estimate the 2-D atmospheric boundary layer flow by reformulating the equations into a spatially continuous, strangeness-free descriptor form of differentiation index 1, following a PPE formulation in conjunction with basis function decomposition.
2) The performance of the proposed reduced-order model and estimator is validated for both synthetic data obtained using LES simulations of the atmospheric boundary layer and real-world LIDAR measurements.

The rest of this brief is organized as follows. Sections II and III constitute the aforementioned contribution, while Section IV provides the relevant results that make up contribution. Concluding remarks are given in Section V.

II. Generalized State-Space Model for Incompressible Flow

Since effects of compressibility become significant only at flow velocities of $M > 0.3$, where M is the Mach number [23], we consider wind flow expressed by the Navier–Stokes equations for viscous incompressible flow [16], [24], as follows:

$$\frac{\partial \mathbf{U}(\mathbf{s},t)}{\partial t} = -\nabla P(\mathbf{s},t) - \mathbf{U}(\mathbf{s},t)\cdot\nabla\mathbf{U}(\mathbf{s},t) + \frac{1}{Re}\nabla^2\mathbf{U}(\mathbf{s},t) \tag{1a}$$

$$0 = \nabla\cdot\mathbf{U}(\mathbf{s},t) \tag{1b}$$

where $\mathbf{U}(\mathbf{s},t)$ and $P(\mathbf{s},t)$ denote the velocity and pressure fields, respectively, evolving over spatial domain $\mathbf{\Omega} \in \mathbb{R}^d$ for d-dimensional flow, with time $t \in \mathbb{R}_+$ and $\mathbf{s} \in \mathbf{\Omega}$. The term Re denotes Reynolds number, the superscript $^\top$ is the transpose operator, and ∇ denotes the del operator. The boundary condition may be specified as

$$\mathbf{U}(\mathbf{s},t) = \mathbf{U}_\delta(\mathbf{s},t) \text{ with } \mathbf{s} \in \delta\mathbf{\Omega} \tag{2}$$

where $\delta\mathbf{\Omega}$ is the domain boundary and the initial condition is

$$\mathbf{U}(\mathbf{s},0) = \mathbf{U}_0. \tag{3}$$

A derivation of the Navier–Stokes equations is given in [25].

It is noteworthy that (1) gives no explicit equation for the pressure P, with a pressure term appearing only once as a spatial derivative on the right-hand side of (1a). In fact,

P is known as a Lagrange multiplier, which enforces the incompressibility of the velocity field $\mathbf{U}$ such that the algebraic equation (1b) is always satisfied. This PDAE system is said to have a higher differentiation index (nondecoupled) since no pressure term exists in the algebraic equation. Furthermore, since the pressure is only determined up to an additive constant, the system is undetermined and the concept of the differentiation index cannot be readily applied [26]. Whenever undetermined solution components exist, the differentiation index concept for general nonlinear DAEs is described in terms of a so-called strangeness index [15]. Consequently, following the strangeness index definition given in [15, Definition 4.4], which is not provided here in the interest of brevity, the above-mentioned system is, after spatial discretization, characterized by a unity strangeness index. To render this formulation amenable to an estimation framework, we propose a reformulation into a strangeness-free spatially continuous generalized state-space form by employing basis function decomposition following a PPE description. The following preliminaries present the necessary matrices and associated invertibility properties required to obtain the main result of this section. Note that all integral operations presented here are performed elementwise.

Let n_ϕ denote the number of basis functions, each $\phi(\mathbf{s}-\boldsymbol{\zeta}_i) : \boldsymbol{\Omega} \to \mathbb{R}$, where $\boldsymbol{\zeta}_i$ is the center of the ith basis function. Furthermore, let $\boldsymbol{\phi}(\mathbf{s}) = [\phi(\mathbf{s}-\boldsymbol{\zeta}_1)\ \phi(\mathbf{s}-\boldsymbol{\zeta}_2)\ \cdots\ \phi(\mathbf{s}-\boldsymbol{\zeta}_{n_\phi})]^\top$ and $\boldsymbol{\phi}(\mathbf{s}) = \mathbf{I}_d \otimes \boldsymbol{\phi}(\mathbf{s})$, where $\otimes$ denotes the Kronecker product operator of two matrices and $\mathbf{I}_d$ is a $d \times d$ identity matrix. The matrix $\boldsymbol{\gamma} \in \mathbb{R}^{dn_\phi \times dn_\phi}$ shall be defined as

$$\boldsymbol{\gamma} \triangleq \int_{\boldsymbol{\Omega}} \boldsymbol{\phi}(\mathbf{s})\boldsymbol{\phi}^\top(\mathbf{s})d\mathbf{s}. \tag{4}$$

Also, define the matrix $\boldsymbol{\eta} \in \mathbb{R}^{n_\phi \times n_\phi}$ as

$$\boldsymbol{\eta} \triangleq \textstyle\int_{\boldsymbol{\Omega}} \boldsymbol{\phi}(\mathbf{s})(\nabla^2\boldsymbol{\phi}^\top(\mathbf{s}))d\mathbf{s} \tag{5}$$

where ∇^2 denotes the Laplace operator. We note that since $\boldsymbol{\gamma}$ is symmetric and positive, then in [27], the matrix is positive definite and hence invertible. To show invertibility for the matrix $\boldsymbol{\eta}$, we consider a regular grid of equally spaced identical basis functions. This yields a Toeplitz-block Toeplitz matrix structure for $\boldsymbol{\eta}$ and its invertibility may be determined in [28] and [29].

In order to obtain a strangeness-free nonlinear descriptor system of differentiation index 1, let

$$\mathbf{f}(\mathbf{U}(\mathbf{s},t), P(\mathbf{s},t)) = \frac{\partial \mathbf{U}(\mathbf{s},t)}{\partial t}. \tag{6}$$

We decompose the spatiotemporal fields $\mathbf{U}(\mathbf{s},t)$ and $P(\mathbf{s},t)$ using an infinite set of linearly independent basis functions $\mathcal{Z} = \{\phi(\mathbf{s}-\boldsymbol{\zeta}_i)\}_{i=1}^{\infty}$, as follows:

$$\mathbf{U}(\mathbf{s},t) = \boldsymbol{\phi}^\top(\mathbf{s})\mathbf{x}(t) \tag{7}$$

$$P(\mathbf{s},t) = \sum_{i=1}^{\infty} \phi(\mathbf{s}-\boldsymbol{\zeta}_i)z_i(t) = \boldsymbol{\phi}^\top(\mathbf{s})\mathbf{z}(t) \tag{8}$$

where $\mathbf{x}(t) \in \mathbb{R}^{dn_\phi}$ and $\mathbf{z}(t) \in \mathbb{R}^{n_\phi}$ are the velocity and pressure state vectors, respectively, that scale the field basis functions $\boldsymbol{\phi}(\mathbf{s})$. Substituting the field decomposition in the momentum equation (1a), we obtain

$$\boldsymbol{\phi}^\top(\mathbf{s})\frac{\partial \mathbf{x}(t)}{\partial t} = \mathbf{f}(\boldsymbol{\phi}^\top(\mathbf{s})\mathbf{x}(t), \boldsymbol{\phi}^\top(\mathbf{s})\mathbf{z}(t)). \tag{9}$$

Premultiplying (9) by $\boldsymbol{\phi}(\mathbf{s})$ and integrating over the spatial domain $\boldsymbol{\Omega}$ yields

$$\int_{\boldsymbol{\Omega}} \boldsymbol{\phi}(\mathbf{s})\boldsymbol{\phi}^\top(\mathbf{s})d\mathbf{s}\ \frac{\partial \mathbf{x}(t)}{\partial t} = \int_{\boldsymbol{\Omega}} \boldsymbol{\phi}(\mathbf{s})\mathbf{f}(\boldsymbol{\phi}^\top(\mathbf{s})\mathbf{x}(t), \boldsymbol{\phi}^\top(\mathbf{s})\mathbf{z}(t))d\mathbf{s}. \tag{10}$$

Substituting $\boldsymbol{\gamma}$ into (10) and premultiplying by $\boldsymbol{\gamma}^{-1}$, we may write

$$\frac{\partial \mathbf{x}(t)}{\partial t} = \boldsymbol{\gamma}^{-1}\int_{\boldsymbol{\Omega}} \boldsymbol{\phi}(\mathbf{s})\mathbf{f}(\boldsymbol{\phi}^\top(\mathbf{s})\mathbf{x}(t), \boldsymbol{\phi}^\top(\mathbf{s})\mathbf{z}(t))d\mathbf{s}. \tag{11}$$

To derive the algebraic equation for $\mathbf{z}(t)$, we first obtain the PPE by taking the divergence of (1a) and using the divergence-free condition of (1b) [30]

$$\nabla^2\ P(\mathbf{s},t) = -\nabla \cdot (\mathbf{U}(\mathbf{s},t) \cdot \nabla\mathbf{U}(\mathbf{s},t)). \tag{12}$$

Let

$$g(\mathbf{U}(\mathbf{s},t)) = -\nabla \cdot (\mathbf{U}(\mathbf{s},t) \cdot \nabla\mathbf{U}(\mathbf{s},t)). \tag{13}$$

Then, substituting the field decomposition into (12) yields

$$(\nabla^2\boldsymbol{\phi}^\top(\mathbf{s}))\mathbf{z}(t) = g(\boldsymbol{\phi}^\top(\mathbf{s})\mathbf{x}(t)). \tag{14}$$

Premultiplying (14) by $\boldsymbol{\phi}(\mathbf{s})$ and integrating over the spatial domain $\boldsymbol{\Omega}$ gives

$$\int_{\boldsymbol{\Omega}} \boldsymbol{\phi}(\mathbf{s})(\nabla^2\boldsymbol{\phi}^\top(\mathbf{s}))d\mathbf{s}\ \mathbf{z}(t) = \int_{\boldsymbol{\Omega}} \boldsymbol{\phi}(\mathbf{s})g(\boldsymbol{\phi}^\top(\mathbf{s})\mathbf{x}(t))d\mathbf{s}. \tag{15}$$

Substituting $\boldsymbol{\eta}$ given by (5) into (15) and premultiplying by $\boldsymbol{\eta}^{-1}$, we have that

$$\mathbf{z}(t) = \boldsymbol{\eta}^{-1}\int_{\boldsymbol{\Omega}} \boldsymbol{\phi}(\mathbf{s})g(\boldsymbol{\phi}^\top(\mathbf{s})\mathbf{x}(t))d\mathbf{s}. \tag{16}$$

The final form of the nonlinear descriptor model may therefore be written as

$$\frac{\partial \mathbf{x}(t)}{\partial t} = \boldsymbol{\gamma}^{-1}\int_{\boldsymbol{\Omega}} \boldsymbol{\phi}(\mathbf{s})\mathbf{f}(\boldsymbol{\phi}^\top(\mathbf{s})\mathbf{x}(t), \boldsymbol{\phi}^\top(\mathbf{s})\mathbf{z}(t))d\mathbf{s} \tag{17a}$$

$$\mathbf{z}(t) = \boldsymbol{\eta}^{-1}\int_{\boldsymbol{\Omega}} \boldsymbol{\phi}(\mathbf{s})g(\boldsymbol{\phi}^\top(\mathbf{s})\mathbf{x}(t))d\mathbf{s} \tag{17b}$$

where both $\mathbf{x}(t)$ and $\mathbf{z}(t)$ are exactly determined, making the formulation strangeness-free. The concept of the differentiation index may now be applied to such system of equations and the formulation is said to have a unity differentiation index.

III. Estimation of the Incompressible Navier–Stokes Equations

A. Reduced-Order Nonlinear DAE Flow Estimation Model

In order to render our flow model apt for estimation purposes, we decompose the velocity and pressure fields using a set of Gaussian basis functions, allowing a finite-dimensional state vector to approximate a spatially continuous field. The field basis functions are described by

$$\phi(\mathbf{s}-\boldsymbol{\zeta}_i) = \exp\left(-\frac{(\mathbf{s}-\boldsymbol{\zeta}_i)^\top(\mathbf{s}-\boldsymbol{\zeta}_i)}{2\sigma_\phi^2}\right) \tag{18}$$

where $\sigma_\phi \in \mathbb{R}$ is a parameter defining the basis function width. The basis function width and placement are computed using a spatial frequency analysis technique that follows the work of Sanner and Slotine [31] and applied in a spatiotemporal context in [32]. This approach considers spatial frequency cutoff as the design parameter describing basis function width and placement.

Since the observations are discrete in time, we discretize time using a first-order Euler method. This simple approach is known to introduce a discretization error [33]; however, this is only incurred in the forward prediction step so it is then corrected throughout the update step of the estimation algorithm. We may write the flow estimation model by first defining $\mathbf{x}_k := \mathbf{x}(k\Delta_t)$ and $\mathbf{z}_k := \mathbf{z}(k\Delta_t)$ with regular time steps Δ_t and denoting the index of the future time sample by the subscript $k+1$.

Substituting the decomposition into (1a) yields

$$\phi^\top(\mathbf{s})\mathbf{x}_{k+1} = \Delta_t \mathbf{f}(\phi^\top(\mathbf{s})\mathbf{x}_k, \phi^\top(\mathbf{s})\mathbf{z}_k) + \phi^\top(\mathbf{s})\mathbf{x}_k + \boldsymbol{\epsilon}_k(\mathbf{s}) \tag{19}$$

where to approximate the effects of model reduction and model uncertainties, the spatial field is subjected to a disturbance $\boldsymbol{\epsilon}_k(\mathbf{s})$, which represents a normally distributed zero-mean white noise process where $\boldsymbol{\epsilon}_k(\mathbf{s}) \sim \mathcal{N}(\mathbf{0}, \sigma_q^2\mathbf{I})$ and the covariance is defined by

$$\operatorname{cov}(\boldsymbol{\epsilon}_k(\mathbf{s}), \boldsymbol{\epsilon}_{k+\tau}(\boldsymbol{\xi})) = \begin{cases} \sigma_q^2\ \delta(\mathbf{s}-\boldsymbol{\xi}), & \text{if } \tau = 0 \\ 0, & \text{otherwise} \end{cases} \tag{20}$$

for all $\tau \in \mathbb{Z}$, where $\boldsymbol{\xi} \in \Omega$, $\mathbf{I}$ is an identity matrix of appropriate dimensions, δ is the Dirac delta function and $\mathcal{N}(\mathbf{0}, \sigma_q^2\mathbf{I})$ denotes the zero-mean normal distribution with covariance $\sigma_q^2\mathbf{I}$. Premultiplying (19) by $\phi(\mathbf{s})$, integrating over the spatial domain Ω and rearranging gives

$$\mathbf{x}_{k+1} = \mathbf{f}^{(\mathbf{x})}(\mathbf{x}_k, \mathbf{z}_k) + \mathbf{q}_k \tag{21}$$

where

$$\mathbf{f}^{(\mathbf{x})}(\mathbf{x}_k, \mathbf{z}_k) = \Delta_t \boldsymbol{\gamma}^{-1} \int_\Omega \phi(\mathbf{s})\ \mathbf{f}(\phi^\top(\mathbf{s})\mathbf{x}_k, \phi^\top(\mathbf{s})\mathbf{z}_k) d\mathbf{s} + \mathbf{x}_k \tag{22}$$

and

$$\mathbf{q}_k = \boldsymbol{\gamma}^{-1} \int_\Omega \phi(\mathbf{s})\boldsymbol{\epsilon}_k(\mathbf{s}) d\mathbf{s}. \tag{23}$$

In [34], we have that $\mathbf{q}_k$ is a zero-mean, normally distributed white noise process with covariance $\mathbf{Q}_k = \sigma_q^2 \boldsymbol{\gamma}^{-1}$. We note that the terms in $\phi(\mathbf{s})$ and its spatial derivatives get integrated and can either be computed analytically or numerically.

Proceeding similarly for algebraic equation (1b), we get

$$\mathbf{z}_k = \mathbf{g}^{(\mathbf{z})}(\mathbf{x}_k) + \tilde{\mathbf{e}}_k \tag{24}$$

where

$$\mathbf{g}^{(\mathbf{z})}(\mathbf{x}_k) = \boldsymbol{\eta}^{-1} \int_\Omega \phi(\mathbf{s}) g(\phi^\top(\mathbf{s})\mathbf{x}_k) d\mathbf{s} \tag{25}$$

where $\tilde{\mathbf{e}}_k$ is a zero-mean, normally distributed white noise process with covariance $\tilde{\mathbf{E}}_k = \sigma_{\tilde{e}}^2 \boldsymbol{\eta}^{-1}$. The discrete-time reduced-order spatiotemporal nonlinear descriptor model is then given by

$$\mathbf{x}_{k+1} = \mathbf{f}^{(\mathbf{x})}(\mathbf{x}_k, \mathbf{z}_k) + \mathbf{q}_k \tag{26a}$$

$$\mathbf{z}_k = \mathbf{g}^{(\mathbf{z})}(\mathbf{x}_k) + \tilde{\mathbf{e}}_k. \tag{26b}$$

We note that the states $\mathbf{x}_k$ and $\mathbf{z}_k$ can be decoupled from the integral computation, thus allowing offline computation and hence more efficient estimation. Following the dimensional analysis carried out in [5], the wind field dynamics over the horizontal plane are largely independent of changes in height, and we will therefore consider only 2-D flow ($d = 2$). Taking the first n_ϕ components of $\mathbf{x}_{k+1}$ as an example and denoting this vector by $\mathbf{x}_{k+1}^{(u)}$ (i.e., the state vector describing the horizontal component of velocity), we may decouple the states from the integral computation, as follows:

$$\begin{aligned} &\mathbf{x}_{k+1}^{(u)} \\ &= \Delta_t \boldsymbol{\gamma}_0^{-1} \Bigg[\frac{1}{Re} \int_{\mathcal{O}} \phi \frac{\partial^2 \phi^\top}{\partial {s_1}^2} d\mathbf{s}\ \mathbf{x}_k^{(u)} + \frac{1}{Re} \int_{\mathcal{O}} \phi \frac{\partial^2 \phi^\top}{\partial {s_2}^2} d\mathbf{s}\ \mathbf{x}_k^{(u)} \\ &\quad - \int_{\mathcal{O}} \phi \frac{\partial \phi^\top}{\partial s_1} d\mathbf{s}\ \mathbf{z}_k - \int_{\mathcal{O}} \phi \left(\phi \otimes \frac{\partial \phi}{\partial s_1} \right)^\top d\mathbf{s}\ \left(\mathbf{x}_k^{(u)} \otimes \mathbf{x}_k^{(u)} \right) \\ &\quad - \int_{\mathcal{O}} \phi \left(\phi \otimes \frac{\partial \phi}{\partial s_2} \right)^\top d\mathbf{s}\ (\mathbf{x}_k^{(v)} \otimes \mathbf{x}_k^{(u)}) \Bigg] + \mathbf{x}_k^{(u)} + \mathbf{q}_k^{(u)} \end{aligned} \tag{27}$$

where $\phi = \phi(\mathbf{s})$, $\mathbf{q}_k^{(u)}$ denotes the first n_ϕ components of $\mathbf{q}_k$, $\mathbf{x}_k^{(v)}$ denotes the last n_ϕ components of $\mathbf{x}_k$, and $\boldsymbol{\gamma}_0$ is given by (4) with $d = 1$. Grouping terms, this equation has the form

$$\mathbf{x}_{k+1}^{(u)} = \mathbf{f}^{(u)}(\mathbf{x}_k, \mathbf{z}_k) + \mathbf{q}_k^{(u)} \tag{28}$$

where

$$\begin{aligned} \mathbf{f}^{(u)}(\mathbf{x}_k, \mathbf{z}_k) &= \mathbf{A}_1 \mathbf{x}_k^{(u)} + \mathbf{A}_2 \mathbf{z}_k + \mathbf{A}_3 (\mathbf{x}_k^{(u)} \otimes \mathbf{x}_k^{(u)}) \\ &\quad + \mathbf{A}_4 (\mathbf{x}_k^{(v)} \otimes \mathbf{x}_k^{(u)}) \\ \mathbf{A}_1 &= \frac{1}{Re} \Delta_t \boldsymbol{\gamma}_0^{-1} \left[\int_{\mathcal{O}} \phi \frac{\partial^2 \phi^\top}{\partial {s_1}^2} d\mathbf{s} + \int_{\mathcal{O}} \phi \frac{\partial^2 \phi^\top}{\partial {s_2}^2} d\mathbf{s} \right] \\ \mathbf{A}_2 &= -\Delta_t \boldsymbol{\gamma}_0^{-1} \int_{\mathcal{O}} \phi \frac{\partial \phi^\top}{\partial s_1} d\mathbf{s} \\ \mathbf{A}_3 &= -\Delta_t \boldsymbol{\gamma}_0^{-1} \int_{\mathcal{O}} \phi \left(\phi \otimes \frac{\partial \phi}{\partial s_1} \right)^\top d\mathbf{s} \\ \mathbf{A}_4 &= -\Delta_t \boldsymbol{\gamma}_0^{-1} \int_{\mathcal{O}} \phi \left(\phi \otimes \frac{\partial \phi}{\partial s_2} \right)^\top d\mathbf{s}. \end{aligned} \tag{29}$$

It is easy to see that the constant matrices $\mathbf{A}_1$, $\mathbf{A}_2$, $\mathbf{A}_3$, and $\mathbf{A}_4$ may be computed offline. By proceeding similarly for any other dimension and component of velocity and pressure, the form of (26) is obtained.

B. Static Pressure Estimation

In the incompressible Navier–Stokes equations (1), the total pressure P appears only as a spatial derivative in the momentum equation (1a). The static ($P^{(s)}$) and dynamic ($P^{(d)}$) pressure terms that make up $P = P^{(s)} + P^{(d)}$ are characterized by different time constants, with $P^{(s)}$ naturally demonstrating much slower dynamics. This makes P unobservable, and

consequently, the pressure estimated using (24) is effectively dynamic pressure. We therefore propose to model static pressure $P^{(s)}$ by a Gaussian random walk model to track its slow variation and take a single pressure measurement $\tilde{y}_k(\mathbf{s}_P) := \tilde{y}(\mathbf{s}_P, k\Delta_t)$ at regular time intervals Δ_t within the spatial domain $\mathbf{\Omega}$. We assume that the static pressure is uniform throughout this domain. The full static pressure model is then given by

$$P_{k+1}^{(s)} = P_k^{(s)} + w_k \tag{30}$$

$$\tilde{y}_k(\mathbf{s}_P) - \phi^\top(\mathbf{s}_P)\mathbf{z}_k = P_k^{(s)} + v_k \tag{31}$$

where $\mathbf{s}_P$ is the position of the pressure sensor, $w_k \sim \mathcal{N}(0, \sigma_w^2)$ and $v_k \sim \mathcal{N}(0, \sigma_v^2 + \phi^\top(\mathbf{s}_P)\mathbf{P}_k^{(z)}\phi(\mathbf{s}_P))$ denote additive white Gaussian noise and $\mathbf{P}_k^{(z)}$ denotes the associated algebraic state covariance matrix. The term $\phi^\top(\mathbf{s}_P)\mathbf{z}_k$ effectively represents the dynamic pressure estimate so the difference between $\phi^\top(\mathbf{s}_P)\mathbf{z}_k$ and the single pressure measurement $\tilde{y}_k(\mathbf{s}_P)$ is used to estimate the static pressure term using the standard Kalman filter. The covariance term of v_k caters to both pressure sensor noise and dynamic pressure estimation error through σ_v^2 and $\phi^\top(\mathbf{s}_P)\mathbf{P}_k^{(z)}\phi(\mathbf{s}_P)$, respectively.

C. Observation Process

Current LIDAR systems can only detect aerosol speeds in the line-of-sight direction of the laser beam. Measurements are taken at discrete points along the line-of-sight path, so we consider the case where observations are available at regular time intervals Δ_t at n_s points distinctly located throughout the spatial domain $\mathbf{s} \in \mathbf{\Omega}$. Define the observation vector as $\mathbf{y}_k(\mathbf{s}_l) := \mathbf{y}(\mathbf{s}_l, k\Delta_t)$. Then, the full model observation equation may be written as

$$\mathbf{y}_k(\mathbf{s}_l) = \mathbf{u}_k(\mathbf{s}_l)\sin\theta + \mathbf{v}_k(\mathbf{s}_l)\cos\theta + \mathbf{r}_k(\mathbf{s}_l) \tag{32}$$

where $\mathbf{u}_k(\mathbf{s}_l) := \mathbf{u}(\mathbf{s}_l, k\Delta_t)$ and $\mathbf{v}_k(\mathbf{s}_l) := \mathbf{v}(\mathbf{s}_l, k\Delta_t)$ are the horizontal and vertical velocity components, respectively, θ is the LIDAR beam half-angle, $\mathbf{s}_l$ is the lth position, and $\mathbf{r}_k(\mathbf{s}_l)$ denotes additive white Gaussian noise having zero mean and covariance $\mathbf{R}_k = \sigma_r^2\mathbf{I}$. Substituting for field decomposition yields the reduced-order model observation equation given as

$$\mathbf{y}_k(\mathbf{s}_l) = \phi^\top(\mathbf{s}_l)\ (\mathbf{x}_k^{(u)}\sin\theta + \mathbf{x}_k^{(v)}\cos\theta) + \mathbf{r}_k(\mathbf{s}_l) \tag{33}$$

where $\mathbf{x}_k^{(v)}$ represents the last n_ϕ components of $\mathbf{x}_k$.

D. Unscented Kalman Filtering for Nonlinear DAE Systems

Since the UKF and most of the state estimation tools do not readily handle nonlinear DAE systems and we cannot treat a descriptor system as a constrained ODE system [14], we make use of a modified UKF algorithm, where the effects of uncertainties and unmodelled dynamics in both difference and algebraic equations may be represented stochastically. In the literature, such uncertainties are typically conveniently represented by zero-mean white Gaussian process noise, such as [5], to account for the effects of assuming 2-D flow and excluding turbine dynamics, and [32], to represent the approximation effects of basis function decomposition. By proceeding similarly for our work, these effects, including those due to time discretisation, are incurred in the forward prediction step. This is then corrected throughout the update step of the estimation algorithm.

State estimation is performed using the reduced-order DAE model given by (26) and (33). Our aim is to find Gaussian approximations to the filtering distribution $p(\mathbf{x}_k, \mathbf{z}_k|\mathbf{y}_{1:k})$ for time steps k running from 0 to K. This is achieved by using an altered UKF algorithm, which follows that proposed by Mercieca *et al.* [35], with a notable difference that the algebraic equation is now stochastic. Consequently, the unscented sampling process required for the state and measurement prediction steps is carried out for the augmented random variable $\mathbf{X}_k = (\mathbf{x}_k^\top\ \mathbf{z}_k^\top)^\top$. Unlike previous approaches, including both differential and algebraic state distributions in the computation of the state and measurement predictions ensures that the estimates use statistical information from all states so that the set of sigma points giving the projected prediction correctly encode the mean and covariance of both differential and algebraic states. Also, instead of obtaining the predicted and filtered algebraic state estimates by directly solving the algebraic equation, the unscented transform is used to compute the mean and covariance of the algebraic state estimates after the differential states undergo the nonlinear transformation $\mathbf{g}$.

As discussed in [5], the coupling between the wind velocity fields is enhanced by assuming that the instantaneous wind direction is uniform throughout the spatial domain under study. Note that since the observation equation is linear in the states, the predicted differential states are corrected using the standard Kalman filter update equations.

IV. Results

This section evaluates the performance of the estimation framework developed here by considering wind flow over a large horizontal plane, using both LES data and real-world LIDAR data. The proposed estimation method gives the full picture of the flow field by using limited sparse flow speed measurements and a single pressure measurement to provide flow velocity and absolute pressure estimates anywhere in the area of interest. This becomes important, for instance, in the detection and prediction of oncoming flow dynamics having length scales smaller than the wind turbine rotor blade diameter, such as wind gusts.

A. Estimation from LES Wind Field Data

Realistic wind field data are generated using the Simulator for Offshore Wind Farm Applications (SOWFA) [24], which enables LES simulations of the atmospheric boundary layer. A typical snapshot of the LES data is shown in Fig. 1 together with a measurement waveform as captured at one measurement point. The LIDAR configuration consists of two beams of half-angle 15° with the line-of-sight wind speed being measured at discrete points along the beams. The LIDAR range considered in this example is 220 m and the distance between sample points (black plus signs) is 20 m, which is considerably less than the characteristic gust length scales ($\mathcal{O}(10^2)$ m) [5].

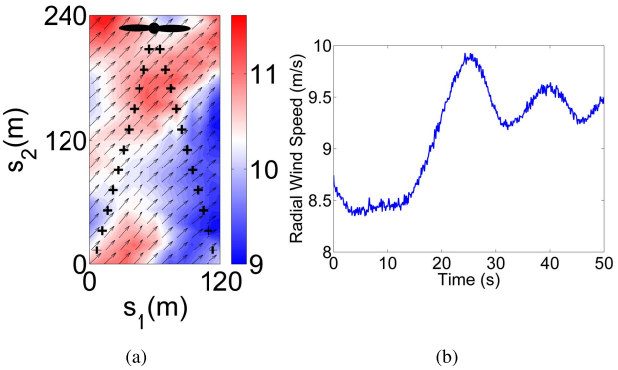

(a) (b)

Fig. 1. (a) Snapshot from an LES of the atmospheric boundary layer together with the line-of-sight wind speed observation locations (black plus signs situated over a 15° half-angle LIDAR beam configuration) within a 120 m × 240 m spatial domain at a height of 100 m above sea level. The contour represents the wind speed in ms^{-1} with the prevailing wind direction being from the southwest. The solid black circle shows the location of the wind turbine nacelle on which the LIDAR unit and pressure sensor are mounted. Note that the rotor blades are shown for clarity, but the turbine dynamics are excluded in this brief. (b) RWS measurement plots as captured at one observation location.

The solid black circle shows the location of the wind turbine nacelle on which the LIDAR unit and pressure sensor are mounted. We shall assume free boundary conditions throughout the estimation process.

1) Basis Function Selection: To ensure that the chosen basis function grid layout can adequately approximate a spatial field, an oversampling parameter of $\rho_\phi = 2.08$ was chosen due to the relatively slow roll-off of Gaussian basis functions, requiring $n_\phi = 15$ basis functions that were equally spaced over a 3×5 grid laid out in the spatial domain $\mathbf{\Omega}$. Consequently, $15 \times 3 = 45$ basis functions are required to represent the velocity and pressure fields.

2) State Estimation: A Monte Carlo approach was used to demonstrate the performance of the proposed state estimation algorithm, where 50 realizations of wind field data were generated. Each realization estimated $K = 500$ data points (in time) with a sample time of $\Delta_t = 0.1$ s. Estimation parameters were set as $\sigma_q^2 = 1\mathrm{m}^2\ \mathrm{s}^{-2}$, $\sigma_{\tilde{e}}^2 = 10^{-4}\ \mathrm{m}^2\mathrm{s}^{-2}$, $\sigma_r^2 = 10^{-3}\ \mathrm{m}^2\mathrm{s}^{-2}$, $\sigma_w^2 = 10^{-5}\mathrm{Pa}^2$, $\sigma_v^2 = 10^{-4}\mathrm{Pa}^2$, $\mathrm{Re} = 10^7$, $\alpha = 1$, and $\beta = 2$. No prior information about initial states was passed on to the state estimator and the initial differential state distribution was set to $\mathcal{N}(\mathbf{0}, 100\boldsymbol{\gamma}^{-1})$.

3) Estimation Performance: The mean root-mean-square error (MRMSE), which is often used in the literature for nonlinear state estimation ([36] and references therein), was used to obtain the accuracy of the resulting state estimates by comparing the estimated field with the generated field. The MRMSE is defined at each time instant k as

$$\mathrm{MRMSE}_k = \frac{1}{N}\sum_{j=1}^{N}\sqrt{\frac{1}{O}\sum_{o=1}^{O}(\nu_{k,o}^{(j)})^2}, k = 0, 1, 2, \ldots, K \tag{34}$$

where $\nu_{k,o}^{(j)}$ is the estimation error at spatial location o at the kth sampling instant for the jth simulation run. O is the number of spatially discrete points (equally spaced on $\mathbf{\Omega}$ with a spatial discretisation step of Δ_s) and N is the number of simulation runs.

TABLE I

AVERAGE MRMSE VALUES FOR THE STABILIZED SIMULATION PERIOD ($t \geq 10$ S) FOR 50 SIMULATION RUNS

Quantity (units)	Value Range [min, max]	RMSE	RMSE(% of range)
Wind speed (ms^{-1})	[6.59, 13.04]	0.72	11.16%
Wind direction (°)	[208.15, 236.66]	2.69	9.44%
Pressure (Pa)	[-27.35, 29.87]	6.17	10.78%

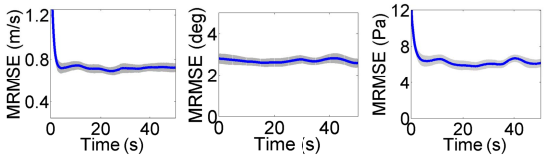

(a) (b) (c)

Fig. 2. Error in the field state estimation. The mean RMSE (solid line) and 95% confidence interval (shaded area) plots are shown for (a) wind velocity magnitude (m/s), (b) wind direction (°), and (c) pressure (Pa).

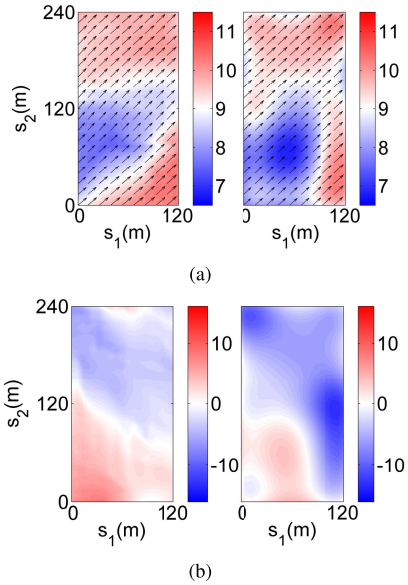

(a)

(b)

Fig. 3. Spatial field estimation is visualized here by showing a single time instant of the generated wind data (left) and estimated flow field (right), shown here for (a) wind velocity magnitude (represented by contours, in m/s) and direction arrows representing direction and (b) pressure (in Pa).

Table 1 summarizes the average MRMSE values for the whole simulation period ($0 \leq k \leq 500$) with Fig. 2 showing the corresponding MRMSE plots. Fig. 3 shows a single time instant of the generated fields and estimated fields. Accurate pressure estimation is obtained despite being measured only at a single point in the field. This shows how the derived reduced-order model and proposed nonlinear descriptor estimation algorithm can identify dynamic pressure and correctly estimate the whole pressure field. The contributions to the estimation errors mainly come from three sources: model uncertainty, model reduction/approximation, and sparse measurements. Although the evolution of wind gusts is a 3-D phenomenon, this work is assuming that the flow is 2-D. Although this is

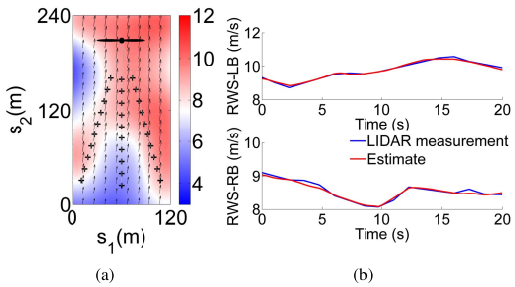

Fig. 4. (a) Single instant from the reconstructed wind field obtained from estimation using the real-world LIDAR wind speed measurements along the two lateral (outer) beams in a 15° half-angle configuration. The wind velocity magnitude is represented by contours (in m/s) and direction arrows represent the wind direction. Note that the rotor blades are shown for clarity, but the turbine dynamics are excluded in this brief. (b) Typical real-world LIDAR wind speed measurement data set shown in comparison with the estimated RWS for the LB (top) and the RB (bottom) at a distance of 80 m away from the LIDAR unit.

not strictly true, it is a reasonable assumption as described and used in [5]. Furthermore, a wind turbine with rotating blades also causes some upstream distortion of the flow as it nears the rotor plane, which is not being modeled in our work. The model reduction scheme employed affects model accuracy and selecting the number of basis functions has to be traded off against the estimation accuracy that can be achieved with limited spatial measurements. Basis function decomposition brings about the loss of high spatial frequency components [37]. The Gaussian approximations made in the UKF-based filtering algorithm also contribute toward the estimation error.

B. Estimation from Real-World LIDAR Measurements

The performance of the proposed estimation framework was further demonstrated for real-world wind speed LIDAR measurements obtained from a five-beam wind turbine-mounted LIDAR unit manufactured by Avent Lidar Technology. Three of the five LIDAR beams provide measurements on a horizontal plane, with two lateral beams at a 15° half-angle and one central beam. Since the only wind field data available is the radial wind speed (RWS) at these observation locations, the two lateral beams are the ones used for estimation, while the central beam is only used for validating the estimation performance. The dynamic wind model and estimation scheme developed here allow for wind field reconstruction of the entire region of interest using these LIDAR measurements. A single instance of this reconstruction is given in Fig. 4(a). The LIDAR observation points are indicated with black plus signs. The LIDAR range is 185 m and the distance between the sample points is 15 m. Basis function selection and state estimation were performed similarly as in Section IV-A, with $\Delta_t = 0.25$s. Numerical tests revealed that the average runtime for the proposed estimation algorithm was 0.083s[1] per single iteration, which comfortably allows for real-time execution.

A comparison of a typical real-world LIDAR data set and its estimate are shown in Fig. 4(b) for the left beam (LB) (top) and the right beam (RB) (bottom) at a distance of 80 m away from the LIDAR unit. A similar comparison is shown in Fig. 5 for every observation location located on the central beam in the order of increasing distance from the LIDAR unit (top to bottom). The accuracy of the state estimates was evaluated by comparing the RWS estimates to the LIDAR wind speed measurements at the central beam, using the MRMSE as defined in (34), where $O = 10$ is now the number of observed spatial locations (along the central beam) and $N = 30$ is the number of independent LIDAR measurement data sets, each of 20-s duration. The MRMSE of the field estimates is shown in Fig. 6(a). The average MRMSE for the entire duration is 0.8452 m/s, which is approximately 12.6% of the wind field RWS range ([5.26 11.95] m/s). This is comparable to the MRMSE value obtained for LES data in Section IV-A, although real-world data now present further uncertainties, including LIDAR range weighting effects and atmospheric stability. Fig. 5 reveals how estimation performance degrades since the measurement points become further spaced apart with distance, leading to a poorer resolution for the underlying basis functions. Detecting wind gusts coming from the furthest locations may be difficult since these may not go past any measurements for them to be identifiable. For practical indications of the expected uncertainty, Fig. 6(b) shows the estimation performance visualized using the MRMSE of the field estimates

[1]Simulations were carried out on an Intel®Core i5-2450M at 2.50-GHz personal computer with 4 GB of RAM.

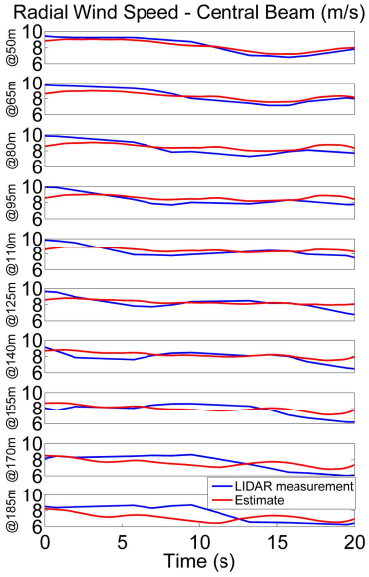

Fig. 5. Typical comparison of the real-world LIDAR wind speed measurements and the corresponding estimation shown for every observation location along the central beam. Plots are shown in the order of increasing distance from the LIDAR unit, with the top plot showing the estimation at 50 m away from the LIDAR equipment.

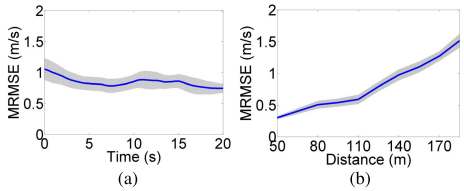

Fig. 6. Error in the field state estimation at the central beam observation locations. The mean RMSE (solid line) and 95% confidence interval (shaded area) are shown for the RWS for 30 independent LIDAR measurement data sets over (a) time and (b) space along the central beam direction.

over distance along the central beam. The MRMSE is defined at each spatial location o as

$$\text{MRMSE}_o = \frac{1}{N}\sum_{j=1}^{N}\sqrt{\frac{1}{K+1}\sum_{k=0}^{K}(\nu_{k,o}^{(j)})^2}. \tag{35}$$

V. Conclusion

This brief has proposed a spatiotemporal wind flow estimation framework with a reduced-order flow model and a nonlinear estimator that accurately estimates velocity and pressure given sparse line-of-sight wind speed measurements. By uniquely employing a PPE formulation, a spatially continuous, strangeness-free nonlinear DAE form of the Navier–Stokes equations was obtained and used for estimation by a modified UKF algorithm. The estimation framework was successfully validated for both simulated and real-world LIDAR data. An average MRMSE of 12.6% was achieved for the estimation of real-world wind data with LIDAR preview distances ranging from 50 to 185 m. For application to the preview control of wind turbines, the recommended preview distance is determined by the blade-pitch system bandwidth [10]. The proposed estimator is yet to be investigated for its benefits in the preview control of wind turbines by implementing the estimator for the modular model predictive control (MPC) layer proposed in [38], which had assumed perfect wind preview knowledge.

Acknowledgment

The authors would like to thank Dr. P. Towers for help with generating wind flow simulation data and Avent LIDAR Technology for providing real-world LIDAR data.

References

[1] D. Schlipf and L. Pao, "Preview control of wind turbines," in *The Impact of Control Technology*, T. Samad and A. M. Annaswamy, Eds., 2nd ed. New York, NY, USA: IEEE Control Systems Society, 2014. [Online]. Available: http://ieeecss.org/sites/ieeecss.org/files/CSSIoCT2Update/IoCT2-RC-Schlipf-1.pdf

[2] N. Wang, K. E. Johnson, and A. D. Wright, "FX-RLS-based feedforward control for LIDAR-enabled wind turbine load mitigation," *IEEE Trans. Control Syst. Technol.*, vol. 20, no. 5, pp. 1212–1222, Sep. 2012.

[3] N. Wang, K. E. Johnson, and A. D. Wright, "Comparison of strategies for enhancing energy capture and reducing loads using lidar and feedforward control," *IEEE Trans. Control Syst. Technol.*, vol. 21, no. 4, pp. 1129–1142, Jul. 2013.

[4] Z. Ma, Z. Yan, M. L. Shaltout, and D. Chen, "Optimal real-time control of wind turbine during partial load operation," *IEEE Trans. Control Syst. Technol.*, vol. 23, no. 6, pp. 2216–2226, Nov. 2015.

[5] P. Towers and B. L. Jones, "Real-time wind field reconstruction from LiDAR measurements using a dynamic wind model and state estimation," *Wind Energy*, vol. 19, no. 1, pp. 133–150, 2016.

[6] F. Dunne, E. Simley, and L. Pao, "Lidar wind speed measurement analysis and feed-forward blade pitch control for load mitigation in wind turbines," Nat. Renew. Energy Lab., Golden, CO, USA, NREL Rep. NREL/SR-5000-52098, 2011.

[7] M. Harris, D. J. Bryce, A. S. Coffey, D. A. Smith, J. Birkemeyer, and U. Knopf, "Advance measurement of gusts by laser anemometry," *J. Wind Eng. Ind. Aerodyn.*, vol. 95, no. 12, pp. 1637–1647, 2007.

[8] L. Y. Pao and K. E. Johnson, "A tutorial on the dynamics and control of wind turbines and wind farms," in *Proc. Amer. Control Conf.*, Jun. 2009, pp. 2076–2089.

[9] G. I. Taylor, "The spectrum of turbulence," *Proc. Roy. Soc. Lond. A, Math. Phys. Eng. Sci.*, vol. 164, no. 919, pp. 476–490, Feb. 1938.

[10] D. Schlipf, D. J. Schlipf, and M. Kühn, "Nonlinear model predictive control of wind turbines using LIDAR," *Wind Energy*, vol. 16, no. 7, pp. 1107–1129, 2013.

[11] Y. Koveos and A. Tzes, "Resonant fluid actuator: Modeling, identification, and control," *IEEE Trans. Control Syst. Technol.*, vol. 21, no. 3, pp. 852–860, May 2013.

[12] R. Wood, "Impact of advanced aerodynamic technology on transportation energy consumption," SAE Tech. Paper 2004-01-1306, 2004.

[13] R. B. Stull, *An Introduction to Boundary Layer Meteorology*, vol. 13. Dordrecht, The Netherlands: Kluwer, 1988.

[14] S. C. Patwardhan, S. Narasimhan, P. Jagadeesan, B. Gopaluni, and S. L. Shah, "Nonlinear Bayesian state estimation: A review of recent developments," *Control Eng. Pract.*, vol. 20, no. 10, pp. 933–953, 2012.

[15] P. Kunkel and V. Mehrmann, *Differential-Algebraic Equations: Analysis and Numerical Solution*. Zürich, Switzerland: EMS, 2006.

[16] M. Soleimanzadeh, R. Wisniewski, and A. Brand, "State-space representation of the wind flow model in wind farms," *Wind Energy*, vol. 17, no. 4, pp. 627–639, Apr. 2014.

[17] M. Aliyu and E. Boukas, "Kalman filtering for affine nonlinear descriptor systems," *Circuits Syst. Signal Process.*, vol. 30, no. 1, pp. 125–142, Feb. 2011.

[18] V. M. Becerra, P. D. Roberts, and G. W. Griffiths, "Applying the extended Kalman filter to systems described by nonlinear differential-algebraic equations," *Control Eng. Pract.*, vol. 9, no. 3, pp. 267–281, Mar. 2001.

[19] S. J. Julier and J. K. Uhlmann, "Unscented filtering and nonlinear estimation," *Proc. IEEE*, vol. 92, no. 3, pp. 401–422, Mar. 2004.

[20] M. Partovibakhsh and G. Liu, "An adaptive unscented Kalman filtering approach for Online estimation of model parameters and state-of-charge of lithium-ion batteries for autonomous mobile robots," *IEEE Trans. Control Syst. Technol.*, vol. 23, no. 1, pp. 357–363, Jan. 2015.

[21] S. Pan, H. Su, Z. Liu, and P. Li, "An unscented Kalman filtering approach for nonlinear singular systems," in *Proc. 11th Int. Conf. Control Automat. Robot. Vision*, Dec. 2010, pp. 485–490.

[22] R. K. Mandela, R. Rengaswamy, S. Narasimhan, and L. N. Sridhar, "Recursive state estimation techniques for nonlinear differential algebraic systems," *Chem. Eng. Sci.*, vol. 65, no. 16, pp. 4548–4556, Aug. 2010.

[23] J. D. Anderson, *Fundamentals of Aerodynamics*, 6th ed. New York, NY, USA: McGraw-Hill, 2017.

[24] M. J. Churchfield, S. Lee, J. Michalakes, and P. J. Moriarty, "A numerical study of the effects of atmospheric and wake turbulence on wind turbine dynamics," *J. Turbulence*, vol. 13, no. 14, pp. 1–32, 2012.

[25] A. J. Chorin and J. E. Marsden, *A Mathematical Introduction to Fluid Mechanics*, 3rd ed. New York, NY, USA: Springer-Verlag, 2000.

[26] J. Weickert, "Applications of the theory of differential-algebraic equations to partial differential equations of fluid dynamics," Ph.D. dissertation, Fac. Math., TU Chemnitz, Chemnitz, Germany, 1997.

[27] C. D. Meyer, *Matrix Analysis and Applied Linear Algebra*. Philadelphia, PA, USA: SIAM, 2000.

[28] I. Gohberg and G. Heinig, "Inversion of finite Toeplitz matrices consisting of elements of a noncommutative algebra," *Convolution Equ. Singular Int. Oper.*, vol. 19, no. 5, pp. 7–46, 2010.

[29] A. Ben-Artzi and T. Shalom, "On inversion of block Toeplitz matrices," *Int. Equ. Oper. Theory*, vol. 8, no. 6, pp. 751–779, Nov. 1985.

[30] D. Rempfer, "On boundary conditions for incompressible Navier–Stokes problems," *Appl. Mech. Rev.*, vol. 59, no. 3, pp. 107–125, May 2006.

[31] R. M. Sanner and J.-J. E. Slotine, "Gaussian networks for direct adaptive control," *IEEE Trans. Neural Netw.*, vol. 3, no. 6, pp. 837–863, Nov. 1992.

[32] P. Aram, V. Kadirkamanathan, and S. R. Anderson, "Spatiotemporal system identification with continuous spatial maps and sparse estimation," *IEEE Trans. Neural Netw. Learn. Syst.*, vol. 26, no. 11, pp. 2978–2983, Nov. 2015.

[33] J. C. Butcher, *Numerical Methods for Ordinary Differential Equations*, 2nd ed. Hoboken, NJ, USA: Wiley, 2008.

[34] M. Dewar, K. Scerri, and V. Kadirkamanathan, "Data-driven spatio-temporal modeling using the integro-difference equation," *IEEE Trans. Signal Process.*, vol. 57, no. 1, pp. 83–91, Jan. 2009.

[35] J. Mercieca, P. Aram, and V. Kadirkamanathan, "Unscented Rauch-Tung-Striebel smoothing for nonlinear descriptor systems," in *Proc. Eur. Control Conf.*, Jul. 2015, pp. 491–496.

[36] Y. Guo and B. Huang, "State estimation incorporating infrequent, delayed and integral measurements," *Automatica*, vol. 58, pp. 32–38, Aug. 2015.

[37] D. R. Freestone, P. Aram, M. Dewar, K. Scerri, D. B. Grayden, and V. Kadirkamanathan, "A data-driven framework for neural field modeling," *NeuroImage*, vol. 56, no. 3, pp. 1043–1058, Jun. 2011.

[38] W. H. Lio, B. L. Jones, and J. A. Rossiter, "Preview predictive control layer design based upon known wind turbine blade-pitch controllers," *Wind Energy*, vol. 20, no. 7, pp. 1207–1226, Jul. 2017.